Elucidating and contrasting the mechanisms for Mg and Ca sulfate ion-pair formation with multi-level embedded quantum mechanics/molecular dynamics simulations

Jan-Niklas Boyn[1] and Emily A. Carter[1,2,3*]

[1]Department of Mechanical and Aerospace Engineering, Princeton University, Princeton, New Jersey 08544-5263, United States
[2]Princeton Plasma Physics Laboratory, Princeton, New Jersey, 08540-6655, United States
[3]Andlinger Center for Energy and the Environment, Princeton University, Princeton, New Jersey 08544-5263, United States
*eac@princeton.edu

Abstract

Solutions and minerals containing sulfate (SO_4^{2-}) and the Ca^{2+} and Mg^{2+} cations are ubiquitous throughout the lithosphere, and are significant components of seawater, thus presenting a prototypical system for the study of strong electrolytes and crystal nucleation mechanisms. However, despite their relative abundance, key questions remain unanswered about the most fundamental atomic-level steps of their mineralization pathways and aqueous dynamics. Here, we carry out enhanced sampling multi-level molecular dynamics (MD) embedded correlated wavefunction theory simulations to elucidate ion-pairing mechanisms for Mg-SO_4 and Ca-SO_4 in concentrated aqueous solution, accurately capturing effects arising from both structural dynamics and electron exchange-correlation. We predict contact-ion-pair formation to be barrierless and highly exoergic for Ca-SO_4, in agreement with its minimal solubility, whereas for Mg-SO_4 solvent-shared and contact ion pairs have similar free energies, qualitatively consistent with its higher solubility. Finally, we demonstrate that brief high-temperature pre-equilibration may be utilized to accelerate convergence of free energies in blue-moon-ensemble enhanced-sampling MD.

1. Introduction

The sulfate anion (SO_4^{2-}) is a significant component of seawater, where it is the second most abundant anion after chloride,[1] and its minerals and salts, particularly of the bivalent cations Mg^{2+} and Ca^{2+}, are abundant throughout the lithosphere, playing key roles in a variety of areas of chemistry, biology, engineering and medicine. $CaSO_4$ has important clinical and biomedical applications, e.g., in bone grafts.[2] Its dihydrate, gypsum, is the most abundant sulfate mineral in

the Earth's crust and has wide-ranging applications in building materials[3-5] and as a plant nutrient.[6] Additionally, its presence is a major cause of fouling in the oil and gas industry,[7, 8] and in desalination and filtration processes,[9] where it can produce difficult-to-remove scales due to its low solubility.[10] On the other hand, aqueous $MgSO_4$ is an archetypical strong electrolyte,[11] which may play a significant environmental role on Earth due to its presence as a common contaminant in mine waters,[12] as well in extraterrestrial environments, having been found, e.g., on Mars[13] and the Jupiter moon Europa.[14]

Despite their ubiquity, uncertainty remains regarding the crystallization pathways of sulfate minerals (gypsum, bassanite, and anhydrite), which may not follow classical nucleation and growth but instead progress via clusters, the structures and properties of which are poorly understood.[15-18] Knowledge of the crystallization mechanism and how it may be influenced could aid development of sustainable technologies, particularly regarding scale inhibition in industrial processes[7, 10] and the development of more durable, weathering-resistant[5, 19-21] and carbon-neutral or -negative building materials.[3, 22, 23] The latter will be a critical strategy for reduction of anthropogenic carbon emissions, with the cement industry alone being responsible for up to 8% of such emissions.[23, 24] Sulfate anions are well known to hinder the crystallization of carbonate minerals such as $CaCO_3$,[25, 26] which serve as long-term sinks for anthropogenic CO_2 in carbon capture, utilization, and storage (CCUS) technologies.[27-31] A particular promising CCUS approach involves processes to remove CO_2 dissolved in seawater, exploiting the ocean's oversaturation with respect to the formation of Mg and Ca carbonate minerals.[32-36] Optimization of such processes requires insight into possible inhibition and competition effects arising from abundant SO_4^{2-} in seawater; however, significant knowledge gaps remain regarding the inhibition of carbonate growth.[37]

Before undertaking characterization of nucleation and growth of the minerals themselves, elucidation of the hydration dynamics and ion-pairing processes of aqueous Mg^{2+}, Ca^{2+} and SO_4^{2-} ions is a necessary foundational first step. Specifically, although the relevant mechanistic uncertainties are largely post-ion-pairing, the simulation of larger-scale crystallization events will require the use of force-fields (FFs), the accuracy of which first should be verified by benchmarking against relevant quantum-mechanics-based simulations of the fundamental atomic-level interactions involved in ion pairing such as we report here. Previous studies of these processes are limited. $MgSO_4$ has been studied experimentally utilizing a variety of spectroscopic

techniques, largely focused on elucidating vibrational signatures and hence the presence of different Mg-SO_4 ion-pair species.[11, 38-46] Some molecular dynamics (MD) studies of $MgSO_4$ have been reported, mostly using classical FFs,[42, 45, 47-50] with quantum mechanics/molecular mechanics (QM/MM)[39] and ab-initio MD (AIMD)[51] simulations being more rare. These theoretical studies largely aimed to reproduce experimental vibrational spectra. To date only a single MD study has reported a free energy curve (FEC) for Mg-SO_4 ion pairing, relying on classical FFs.[52] For Ca-SO_4, experimental research has centered on understanding non-classical nucleation pathways,[26, 53-56] with only one MD investigation of the energetics of ion pairing that employed classical FFs as well as density functional theory (DFT) MD.[57]

Motivated by the relative dearth of ab-initio level understanding of the energetics of sulfate interactions with alkaline earth cations in aqueous solution, here we present multi-level embedded correlated wavefunction (ECW) theory[58-61] calculations in combination with enhanced sampling DFT-MD simulations to elucidate the FECs for Ca^{2+} and Mg^{2+} ion pairing with SO_4^{2-}. While theory and experiment both suggest overall Ca^{2+}-SO_4^{2-} ion pairing in water is entropically driven,[62] elucidating the mechanism and free energies of interconversion between different close-contact ion-pair configurations will benefit from accurate description of changes in chemical bonding, especially because entropic differences between different ion-pair configurations could be small. The DFT-MD/ECW methodology allows for the simultaneous treatment of effects arising from structural dynamics and many-electron exchange-correlation (XC), both which we have shown are essential for accurately evaluating the free energetics of aqueous carbon dioxide speciation,[63] as well as ion pairing and dehydration processes.[64, 65] Here, our aim is to understand at the atomic level why and how the ion-pairing mechanisms of aqueous Ca and Mg sulfate differ, and how they correlate with the observed solubilities (the former is extremely insoluble while the latter readily dissolves). Moreover, in the context of seawater-based CCUS and our previous work on Mg^{2+} and Ca^{2+} dehydration dynamics[65] and carbonate ion-pairing,[64] we hope to gain insights into the competition in ion pairing between different anions, which could be critical to understanding the inhibition of proposed non-classical nucleation pathways in carbonate and sulfate minerals involving pre-nucleation clusters.[66-68] Finally, as efforts are being made to derive FFs for ions present in seawater and those with important biological functions,[69] ab-initio reference data such as that generated here can help confirm or dispute findings obtained with classical FFs.

2. Methods

2.1. Periodic DFT-MD Simulations

We performed Born-Oppenheimer DFT-MD simulations with periodic boundary conditions (PBCs) as implemented in the Vienna Ab-initio Simulation Package (VASP), version 6.3.2.[70-72] The revPBE XC functional[73] with the D3BJ dispersion correction[74, 75] was employed, based on its ability to correctly reproduce the structure of liquid water.[76] All-electron, frozen-core, projector augmented-wave (PAW) potentials[72, 77] were utilized with a planewave (PW) kinetic energy cutoff of 660 eV. This PW cutoff converges the total energy of the simulation supercell to ~1 meV/atom. The Mg and Ca ions PAW potentials used treat the semicore s and p and the valence states self-consistently (denoted *Mg_sv* and *Ca_sv* in the VASP library), while standard PAW potentials represented the nuclei plus all core electrons of the S, O, and H atoms (*S*, *O, H* in the VASP library). Gaussian smearing of 0.1 eV was applied. The Nosé-Hoover thermostat,[78, 79] with a Nosé mass corresponding to a temperature oscillation frequency with a period of 40 MD timesteps, was employed for NVT-ensemble MD simulations at 300 K.

The physical model consisted of a cubic simulation cell with identical side lengths of 12.795 Å, containing one Mg^{2+} or Ca^{2+} cation, one SO_4^{2-} anion, and 67 water molecules. The size of the supercell was chosen to represent the experimental density of water at room temperature. Because of the scaling limitations of AIMD, this supercell does not allow for the simulation of fully separated ions, and thus computation of the true standard free energy of ion pairing from separated ions is not possible. It does, however, allow for the simulation of different ion-pairing modes. No spurious formation of ion-pair chains across periodic boundaries is observed, with the different ion-pairing modes investigated remaining well separated from their periodic images on the timescales of our simulations. Nonetheless, we do note that there may be solvent-separated interactions due to the Bjerrum length for divalent ion pairs being larger than the simulation cell. Initial structures were generated based on a smaller supercell model used previously to study the dehydration dynamics of Mg and Ca cations and their ion-pairing mechanisms with carbonate.[64, 65] The dimensions of these supercells were scaled by a factor of 1.25, and the carbonate anion was replaced by SO_4^{2-}, placed in a solvent-separated ion pair (SSIP) configuration along the supercell diagonal (*vide infra*), and an additional 14 waters were added. This new supercell was relaxed using steepest-descent for 500 ionic steps, followed by DFT-MD pre-equilibration for 5 ps using

0.5-fs timesteps. The final structure from this pre-equilibration trajectory was chosen as the initial configuration for production simulations, which utilized 0.25-fs timesteps.

The free-energy curves (FECs) for the ion-pairing processes were obtained using blue-moon ensemble (BME)[80] constrained MD simulations (BME-MD), with constraints enforced using the SHAKE algorithm.[81] BME-MD is chosen for enhanced sampling as it readily lends itself to our ECW theory simulations (*vide infra*). Because in BME-MD all critical points are sampled with independent trajectories, snapshots are readily obtained at equally spaced points along the production simulation. Identification of well-separated snapshots at each of the critical points is less intuitive for other rare-event sampling methods such as umbrella sampling or metadynamics. BME gradients were integrated using the scipy.integrate python module.[82] The Mg/Ca – S distance (R(M-S)) was defined as the reaction coordinate (RC) and discretized into sets of distinct values of R(M-S) (*vide infra*). Initial configurations for each value of R(M-S) were obtained via slow-growth simulations[83] initiated from the final configuration of the equilibrium MD trajectory discussed below (a solvent-shared ion pair (SSHIP) for Ca and a SSIP for Mg). This single collective variable BME-DFT-MD scheme was used previously to model ion pairing of Mg-CO_3, yielding results consistent with 2D sampling simulations, lending credence to this 1D sampling approach, at least for that system.[64] Active sampling of orthogonal degrees of freedom, such as the coordination number (CN), were found to be important when using metadynamics to simulate ion-pairing energetics involving Mg^{2+} but such 2D sampling is not tractable within BME-DFT-MD. How we overcome this limitation, namely ensuring equilibration of the coordination environment of the Mg^{2+} cation in the BME-MD simulations, is discussed in detail in the Results & Discussion section.

2.2. ECW Theory Simulations

Following BME-MD simulations, ECW theory[58, 59, 61] was used to correct for errors in the electronic energy contribution to the ion-pairing free energy[60] obtained from PBC-DFT-revPBE-D3BJ-MD simulations. This correction is necessary because pure generalized gradient approximation (GGA) XC functionals produce charge-delocalization artifacts,[84] which may result in sizeable errors in ion-pairing free energies.[64] For the ECW simulations, the system is divided into a so-called *cluster*, which comprises the ions directly involved in the reaction and their first solvation shells, i.e., $Mg(SO_4)(H_2O)_{14}$, $Ca(SO_4)(H_2O)_{16}$, while the remaining water molecules define the *environment.* The Ca cluster contains an additional two waters compared to the Mg

cluster because of the Ca^{2+} cation's ability to access six-, seven-, and eight-coordinate environments (Mg^{2+} cannot expand its coordination shell beyond six). We then utilize density functional embedding theory (DFET),[58, 61] implemented in a modified version of VASP 6.3.2 (open-source and available on *github*),[85] to derive embedding potentials (V_{emb}) that account for the interaction between the cluster and its environment. The embedding potentials then are transformed from a real-space grid, obtained from PBC-DFT calculations, into the given Gaussian-type-orbital (GTO) basis set for ECW theory calculations using the open-source, in-house-developed *EmbeddingIntegralGenerator*.[86]

In the present framework, a correction to the PBC-DFT-revPBE-D3BJ energy of a given critical point on the FEC is obtained from:[63]

$$F_{ECW}^{MD} = F_{revPBE+D3BJ}^{MD} + \sum_{j=1}^{k} \frac{\left(E_{ECW}^{I}[V_{emb}] - E_{revPBE+D3BJ}^{I}[V_{emb}]\right)_j}{k} = F_{revPBE+D3BJ}^{MD} + \bar{\delta}_{emb}$$

where $F_{revPBE+D3BJ}^{MD}$ is the free energy obtained from the PBC-DFT-revPBE-D3BJ BME-MD simulation, $E_{ECW}^{I}[V_{emb}]$ is the MP2[87, 88] total energy of the *cluster* obtained in the presence of V_{emb} in a chosen GTO basis set, $E_{revPBE+D3BJ}^{I}[V_{emb}]$ is the DFT-revPBE-D3BJ energy of the *cluster* obtained in the presence of V_{emb} in the same GTO basis. For each critical point on the BME-MD FEC, the sum here runs over eight equally spaced snapshots along the constrained MD trajectory, yielding an average ECW correction to the BME-MD free energy, $\bar{\delta}_{emb}$. All GTO-based calculations utilized the def2-TZVP basis set[89] and were carried out in Molpro version 2021.2.[90] The embedding potential is accounted for in the Molpro calculations using its MATROP routine, which allows V_{emb} to be added as an external potential to the 1-electron integrals. The choice of MP2 as the ECW method is based on previous benchmarking on simulations of aqueous Ca^{2+} and Mg^{2+} cation dehydration dynamics, which showed MP2 yielded comparable accuracy to CCSD(T).[65]

3. Results and Discussion

3.1. Equilibrium MD Simulations

We first present results of unconstrained equilibrium MD simulations meant to elucidate and contrast the equilibrium behavior of the concentrated (~0.8 M) Mg and Ca sulfate solutions. Note that for $CaSO_4$, this is a supersaturated, non-equilibrium concentration that is not

experimentally accessible. However, studying elementary ion-pairing processes at the AIMD level requires these higher concentrations due to cell-size limitations resulting from the expense of DFT calculations. In principle, one would expect to observe a spinodal decomposition at such supersaturation, but this phenomenon is suppressed because only one ion pair is present in the simulation cell. The trajectories were initialized as SSIPs (cation-sulfur distances of ~7 Å), placed along the diagonal of the supercell, as mentioned earlier. Data were collected over production simulations of 50 ps at 0.25-fs timesteps for both systems. The M-S distance was monitored throughout the course of the simulations (Figure 1a). In the case of Mg^{2+}, no significant changes to R(M-S) were observed on the 50-ps timescale of the simulation, with minor fluctuations around the 7-Å distance at which it was initialized, suggesting that ion pairing isn't an extremely facile process for Mg^{2+}, consistent with the known slow water-exchange times around Mg^{2+}.[65, 91-93] A different picture is observed for Ca^{2+}, where after ~17 ps of simulation a drop in R(M-S) from ~7 Å to 5.5 Å occurs, corresponding to the formation of a SSHIP (*vide infra*), followed by another drop in R(M-S) to ~4.5 Å in the final 3 ps of the simulation. Consistent with their general hydration properties – Mg^{2+} and SO_4^{2-} are strongly solvated, Ca^{2+} less so[39, 94] – this equilibrium simulation suggests more facile cation-anion association in the case of Ca^{2+}. However, enhanced-sampling simulations (detailed below) are required to interrogate this phenomenon further due to the limited timescales accessible to equilibrium AIMD.

We also monitored the coordination environments of the two cations by computing their CNs along the trajectory (Figure 1b), defined by the conventional switching functions[95] $\zeta = \sum_{i=1}^{N} \left. 1 - \left(\frac{R_i}{c}\right)^a \middle/ 1 - \left(\frac{R_i}{c}\right)^b \right.$, where i runs over all M-O bonds, R_i is the length of bond i, the exponents a and b take the values of 10 and 28, respectively, chosen to yield integer CNs, and c is chosen to be the minimum in the M-O pair correlation function (PCF) between the first and second coordination-shell peaks, taking values of 3.2 Å and 3.4 Å for Mg^{2+} and Ca^{2+}, respectively. Both cations were initialized in their six-coordinate equilibrium geometries. As mentioned earlier, aqueous Ca^{2+} has stable six-, seven-, and eight-coordinate configurations; these states are separated by low barriers that should render all three configurations accessible on the timescales of our simulations.[65] Mg^{2+} remains hexacoordinate throughout the simulation, consistent with earlier analogous simulations, which found that the charge-dense Mg^{2+} cation is unable to expand its solvation shell and dehydration must surmount a nontrivial barrier (~0.3 eV at this level of

theory,[65] 0.41 eV measured by experiment,[91] in neutral solution). On the other hand, the larger and less charge-dense Ca^{2+} cation can undergo facile water exchange and an increase in the CN to 7 is observed around ~17 ps, coinciding with SSHIP formation, suggesting that these processes may be synergistic.

Inspection of the M-O and S-O PCFs (Figure 1c, d) reveals the expected, minor differences in the former for Ca^{2+} and Mg^{2+}, while the latter are identical for the two cations. For both Ca^{2+} and Mg^{2+}, two strong peaks are visible in the M-O PCF, corresponding to the cations' first and second hydration shells. These peaks are shifted to slightly larger M-O distances for the larger, less charge-dense Ca cation. The locations of the first two M-O peaks (Ca-O: 2.40 Å, 4.52 Å; Mg-O: 2.10 Å, 4.30 Å) agree with previous studies of the dehydration dynamics of Ca and Mg cations in neutral and alkaline solutions,[65] and lie within measured ranges.[96, 97] The identical S-O PCFs for the two systems indicate that the cation has negligible impact on the solvation environment of the sulfate anion over the limited timescales sampled. The locations of the two S-O peaks (Ca, S-O: 1.50 Å, 3.72 Å; Mg, S-O: 1.50 Å, 3.76 Å), corresponding to the S-O bonds in sulfate and the location of its first hydration shell, are consistent with the hydration shell distances measured by X-ray diffraction[38, 98-101] and large-angle X-ray scattering[102] (3.67 – 3.89 Å and 3.61 Å, respectively), as well as with prior classical FF-MD and QM/MM simulations (3.72 - 3.82 Å).[52, 102, 103]

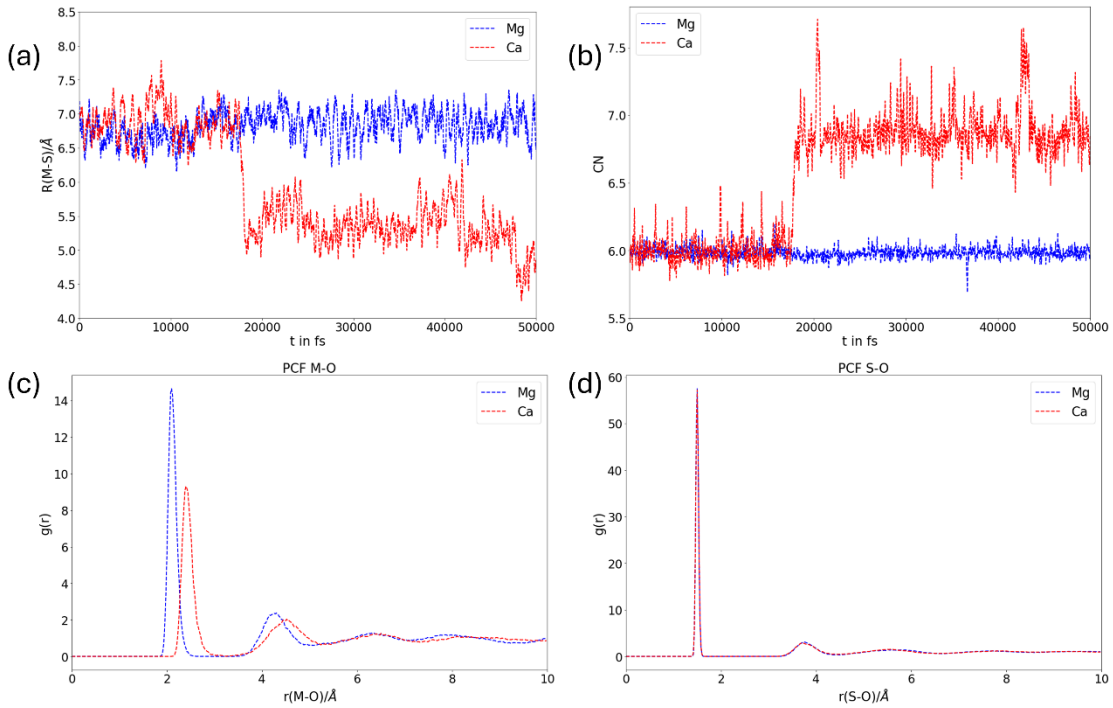

Figure 1. Data from unconstrained, 50-ps DFT-revPBE-D3BJ-MD simulations of the Mg/Ca(SO$_4$)(H$_2$O)$_{67}$ systems. Ca data are in red, Mg in blue. Evolution along the trajectory of the (a): Mg/Ca-S distance and (b) Mg/Ca-O CN. (c) Mg/Ca-O PCF and (d): S-O PCF; both (c) and (d) are averaged over the 50-ps trajectory.

3.2. Constrained BME-MD Simulations

Because the slow nature of ion-pair formation makes it inaccessible within traditional, equilibrium AIMD simulations, we conducted enhanced-sampling BME-MD simulations to generate the FECs for ion pairing to form (Ca/Mg)SO$_4$ in water. As noted earlier, the limitation placed on the simulation cell size by the computational scaling of AIMD motivates particular focus on the SSHIP to CIP region, as the cell size is too small to model larger ion-pair separations. The configurations in this region remain well separated from their periodic images along the trajectories. The R(M-S) RC was discretized into 24 (Ca) and 25 (Mg) values (in Å) connecting the SSIPs with the contact ion pairs (CIPs): For Ca: [2.60, 2.80, 2.98, 3.10, 3.20, 3.30, 3.40, 3.50, 3.60, 3.70, 3.80, 3.90, 4.00, 4.10, 4.25, 4.50, 5.00, 5.25, 5.50, 6.00, 7.00, 7.50, 8.00] and for Mg: [1.82, 2.00, 2.20, 2.40, 2.60, 2.70, 2.80, 2.90, 3.00, 3.10, 3.25, 3.35, 3.50, 3.62, 3.75, 3.87, 4.00, 4.50, 5.00, 5.50, 6.00, 6.50, 7.00, 7.15, 7.50]. The creation of initial structures via slow-growth simulations, in which one coordinate advances as a constrained linear interpolation between initial and final states while all other coordinates evolve according to their forces, can place the system in unfavorable, non-equilibrium coordination environments. The

potentially poor initial guess structures for the FEC, coupled with the strongly hydrated nature of the ions, may result in long pre-equilibrium periods and slow convergence of the energetics as the coordination environment of the cations cannot be actively sampled easily with AIMD. Evidence of this problem is illustrated in the SI (Figure S1a), in which FECs obtained from traditional continuous integration over the trajectories exhibits very slow convergence due to the poor initial guesses (*vide infra*). Thus, we instead generate FECs by averaging over 5-ps trajectories at successively later start and stop times along the trajectory, "interval integration". We checked the FECs and individual BME gradients of the RC points for convergence after each successive 5-ps interval of simulation time. Note that we do not expect the 5-ps intervals to be long enough to, e.g., observe water-exchange around Mg^{2+}. Instead, intervals of 5 ps are chosen as they are sufficiently long to average out thermal fluctuations occurring on short timescales while being short enough to reveal sustained changes in FECs due to equilibration of the coordination environment. These 5-ps intervals simply serve as data gathering intervals along the longer trajectory. Consistent shifts in one direction in successive 5-ps interval FECs are indicative of sustained changes due to equilibration, allowing for accurate identification of the pre-equilibration period, which is then excluded from the period defining the production simulations utilized for analysis. The FECs obtained from this systematic approach to determining the appropriate pre-equilibration period and subsequent averaging time are compared to those obtained from traditional continuous integration over the trajectories, in 5-ps increments in the SI (Figure S1a,b). The difference between two sets of curves clearly demonstrates how successive interval integration aids in the identification of BME convergence.

For the Ca-SO_4 system, initial 15-ps trajectories for each of the 24 values of R(Ca-S) were simulated (totaling 360 ps). In our previous simulations of (Ca/Mg)-CO_3 ion-pairing, convergence of the FEC was achieved on this timescale. However, inspection of the successive 5-ps FECs (Figure 2a) reveals non-convergence of the BME gradients (which integrate to give the FEC) after 15 ps. Considering the significant computational resources required to converge the entire FEC for R(Ca-S) from 2.6 Å to 8.00 Å, and the limitations imposed by the supercell size, subsequent simulations then were conducted only for the region of the FEC connecting the CIPs with the SSHIP. Consequently, a subset of 15 R(Ca-S) values ([2.98, 3.10, 3.20, 3.30, 3.40, 3.50, 3.60, 3.70, 3.80, 3.90, 4.00, 4.10, 4.25, 4.50, 5.00], Å) was simulated for a further 20 ps, for a total of 35 ps for each point and 660 ps of overall simulation time for the Ca-SO_4 system.

Integration of successive 5-ps windows for the SSHIP to CIP portion of the FEC (Figure 2b) yields better convergence after 15 ps. The BME FEC thus integrated over 20 ps, discarding the first 15 ps as equilibration, is shown in red.

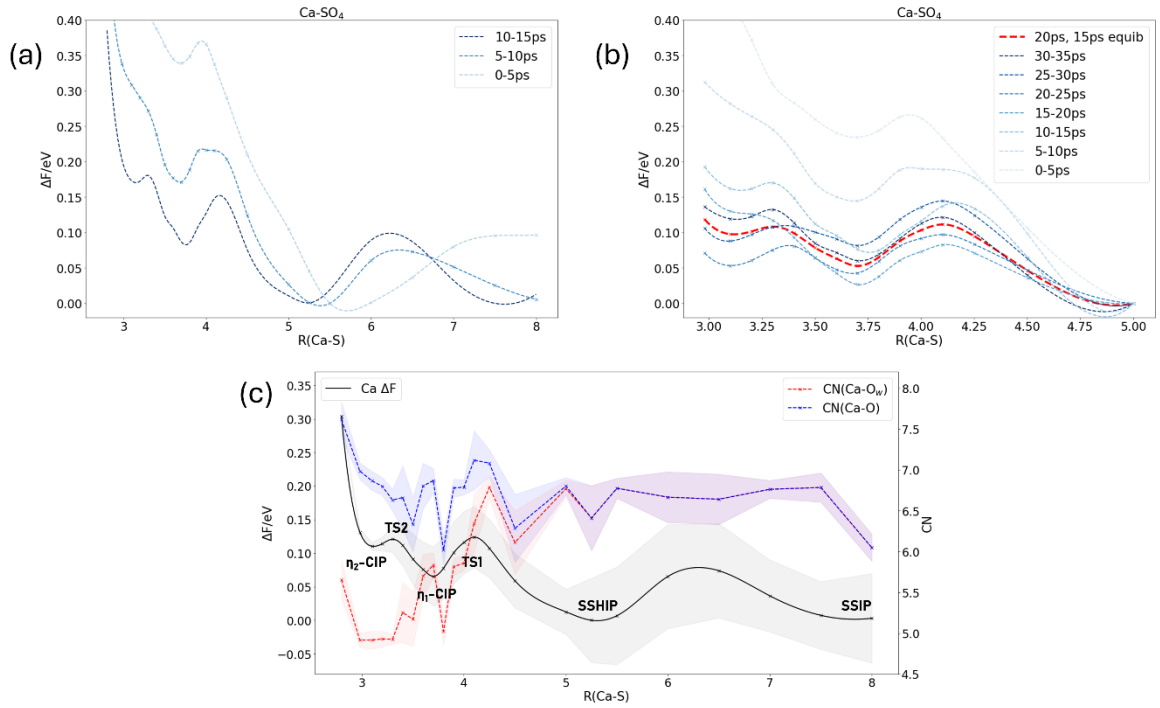

Figure 2. FECs obtained by integrating over successive 5-ps intervals from constrained BME-MD simulations at 300 K for Ca-SO4 ion pairing, covering R(Ca-S) values (a): from 2.60 to 8.00 Å and (b): from 2.98 to 5.00 Å. (c): Final composite FEC (left axis, black curve) created from 20-ps simulations following 15 ps of equilibration for R(Ca-S) from 2.98 to 5.00 and 10-ps simulations following 5 ps of equilibration for R(Ca-S) points outside this range. The shaded area denotes the standard deviation of the free energy computed from the average free energies of each successive 5-ps integration interval along the 20-ps production trajectories at each point on the FEC. The Ca-O CN (right axis) for all oxygens (CN(Ca-O), blue line) and only water oxygens (CN(Ca-Ow), red line), averaged over the post-equilibration trajectories, and their standard deviations computed across all production simulation configurations (shaded areas).

We obtained a final FEC by combining the 20-ps trajectories following 15 ps of pre-equilibration for the SSHIP-CIP region, with 10-ps trajectories following 5 ps of pre-equilibration for the remaining R(Ca-S) points lying outside of this region (R(Ca-S) < 2.98 Å, R(Ca-S) > 5.00 Å). The points with R(Ca-S) > 5.00 Å exhibit inherently higher uncertainty due to possible spurious interactions with periodic images at long R(Ca-S). Moreover, that part, as well as the R(Ca-S) < 2.98 Å part, of the FEC are not the focus of this work, thus warranting shorter trajectories. This final FEC (Figure 2c), shows roughly degenerate SSIP and SSHIP states (subject to the uncertainties just discussed), separated by a low barrier of 0.08 eV, and a positive reaction free energy for CIP formation. The monodentate CIP (η_1-CIP) lies 0.07 eV above the SSHIP state, with a barrier to formation (TS1) of 0.12 eV. The bidentate CIP (η_2-CIP) exhibits a

very shallow minimum at 0.11 eV relative to the SSHIP reference, with a forward barrier of 0.06 eV for conversion from the η_1-CIP. These values are similar to those previously reported from metadynamics simulations utilizing DFT-BLYP-D3-MD,[57] which agree with our results to within ±1 kcal/mol.

Figure 2c also shows the evolution of the Ca-O and Ca-O_w CNs along the reaction path, the latter denoting the CN between Ca and water oxygens only. Following initiation as a hexacoordinate ion, Ca^{2+} assumes a heptacoordinate solvation shell during the SSIP-to-SSHIP transition. At the SSHIP minimum, facile interconversion between six and seven coordinate environments occurs, with an average CN of ~6.5. From this point onwards along the ion-pairing coordinate, multiple coordination environments are accessed as waters directly bound to the Ca^{2+} cation are replaced by SO_4^{2-} oxygens. The CN(Ca-O) increases to an average of 7 at the TS connecting the SSHIP (TS1) with the η_1-CIP as Ca^{2+} expands its coordination shell. Once the TS1 barrier is crossed, CN(Ca-O_w) and CN(Ca-O) diverge. Interestingly, Ca-O_w falls to 5.0 as two waters are lost from Ca^{2+}'s first hydration shell during formation of the first Ca-O_s bond (O_s refers to an O in SO_4^{2-}), before another water again joins the first solvation shell at the η_1-CIP, which is on average seven-coordinate, with six water ligands. The transition to the η_2-CIP proceeds via a later transition state, where a water ligand is lost before passing the TS2 barrier, with the Ca cation largely remaining six-coordinate while crossing the barrier. Once the bidentate sulfate is bound to Ca cation, its CN rises again to seven. Agreement of the previously reported metadynamics simulations, which utilized 2D sampling, employing the Ca-O CN as an additional RC, with our BME-MD results utilizing R(Ca-S) as the sole RC, suggests that water-exchange around the Ca^{2+} and SO_4^{2-} ions is well captured by BME-MD at the 35-ps timescale.

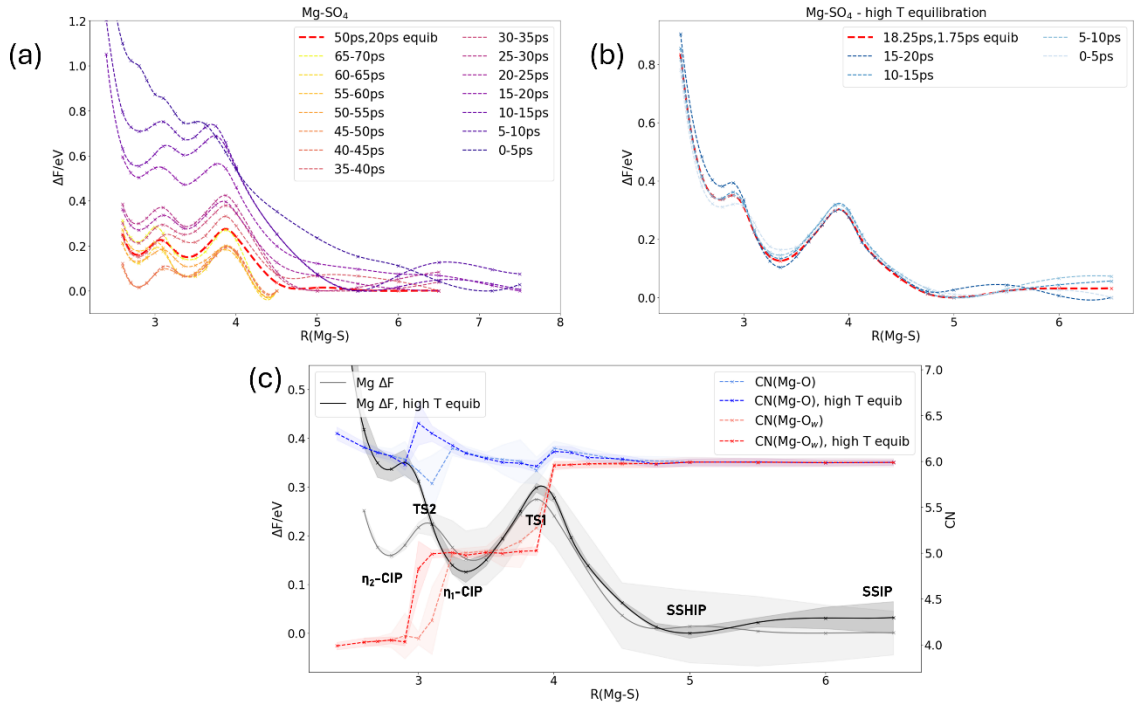

Figure 3. (a): FECs obtained by integration over successive 5-ps intervals from constrained BME-MD simulations at 300 K for Mg-SO4 ion pairing, covering R(Mg-S) values from 1.82 to 7.50 Å. The number of R(Mg-S) points was successively reduced with increasing simulation time, focusing on the SSHIP-to-CIP transition, for the sake of computational tractability. The red curve denotes the final composite FEC obtained from 50 ps of simulation following 20 ps of equilibration for R(Mg-S) from 2.6 to 4.5 Å, and 20 ps of simulation following 20 ps of equilibration for 5 to 6.5 Å. (b): FECs obtained by integration over successive 5-ps intervals from constrained BME-MD simulations at 300 K following 1.25 ps of pre-equilibration at 370 K for Mg-SO4 ion pairing, covering R(Mg-S) values from 2.40 to 6.50 Å. The red curve denotes the final FEC obtained from 18.25 ps of simulation time following 1.75 ps of equilibration, all at 300 K, starting from the structure at the end of the 370-K 1.25 ps trajectory. (c): Comparison of the final FECs for the two sampling approaches (red curves of (a) and (b); left axis, black and grey lines). The shaded areas denote the standard deviation of the free energy computed from the average free energies of each successive 5-ps integration intervals along the 50-ps production trajectories. Mg-O CNs for all oxygens (CN(Mg-O), blue lines) and only water oxygens (CN(Mg-Ow), red lines), averaged over the post-equilibration trajectories at each point on the FEC, and their standard deviations, computed across all production simulation configurations (shaded areas) (right axis). Data obtained from the high-T pre-equilibrated trajectories denoted by darker colors.

For the Mg-SO4 system, even slower convergence is observed for the BME-MD FEC. Initial trajectories were simulated for 10 ps, covering R(Mg-S) from 1.82 Å to 7.5 Å, discretized into 25 points, after which the shortest R(Mg-S) values of 1.82 Å, 2.00 Å, and 2.20 Å were removed from the trajectory set due to clear inaccessibility of these states. The simulations were continued in further 5-ps increments and the simulation set of R(Mg-S) values was successively refined to focus on the region critical to understanding the SSHIP to CIP transformation. The set of 14 distances between 2.6 Å and 4.5 Å was simulated for a total of 70 ps per trajectory. The total simulation time across all points and trajectories sum to 1.265 ns. As becomes obvious from

the successive 5-ps interval BME-MD FECs (Figure 3a), Mg-SO_4 exhibits extremely slow convergence, with significant variation remaining between successive 5 ps trajectories even after 70 ps of total simulation time. Uncertainty remains regarding both the barrier to CIP formation from the SSHIP, and the relative stability of the mono- and bi-dentate CIP modes, with the latter increasing in relative free energy during the final stages of the simulations. Note that we could not resolve a minimum for a tridentate coordination mode, which had been found with classical FF-MD.[52]

This slow convergence behavior is likely the result of slow water exchange around the charge-dense Mg^{2+} cation, which exhibits a large barrier to dehydration,[65, 91-93] in addition to strong solvation of the SO_4^{2-} anion. For example, there is a large shift between successive FECs < 20 ps and > 20 ps in Figure 3a, which coincides with a dehydration event of the Mg^{2+} cation at TS1 (cf. light blue line for the CN before and after 20 ps in Figure S2 in the SI). Significantly faster convergence of the BME-MD surfaces was observed for simulations of dehydration of Mg^{2+} alone,[65] as well as for Mg-CO_3 ion pairing,[64] hence, the slow convergence of the Mg-SO_4 system is likely a compounding effect of these two factors. If the initial structure for each value of R(Mg-S), generated from slow-growth simulations initiated at the SSIP, places either the Mg^{2+} cation or SO_4^{2-} in an unfavorable coordination environment, relaxation into their equilibrium environment may not be possible on timescales accessible to AIMD. This issue may be overcome by utilizing CN(Mg-O) as an additional coordinate to be sampled, elucidating a 2D free energy surface (FES) for the ion-pairing reaction. However, such 2D sampling is not feasible within AIMD for the entire range of R(Mg-S).

Note that in contrast to other rare-event sampling methods such as metadynamics, in which the RC is biased to access different values along a single trajectory, in BME-MD each discretized R(Mg-S) value is simulated with a distinct trajectory in which all other degrees of freedom, such as the CN, are free to equilibrate. Although water-exchange times for Mg^{2+} cation in its equilibrium environment are beyond those accessible to AIMD, the BME-MD trajectories, e.g., around the TSs, place the Mg^{2+} cation in high-energy, non-equilibrium configurations with partially broken/formed ligand bonds. Water exchange is probably faster in such configurations. Indeed, we see significant changes in CN(Mg-O) along the constrained trajectories (Figures S2 and S3), which coincide with shifts in the FECs. This same approach was applied successfully to Mg-CO_3 ion-pairing.[64] However, while water-exchange events are observed along the BME-MD

trajectories for Mg-SO_4, convergence remains slow and uncertainty remains regarding sufficient sampling of the orthogonal degrees of freedom.

Hence, to overcome these sampling limitations, we investigate the effect of using a short high- temperature pre-equilibration period, which may allow the Mg-SO_4 system to escape any local minima in which it may be trapped. As an initial investigation, we considered the TS1 structure, which was slowly converging in the 300-K-only simulations. Instead, a 1.25-ps, 370-K simulation starting from the TS1 structure obtained from slow-growth simulations at 300 K produced a final configuration that was used to initialize a new 20-ps, 300-K trajectory. The evolution of the BME-MD gradients and CNs for the new high-temperature, pre-equilibrated simulation and the original simulation are compared in the SI (Figure S2). Inspection reveals that high-temperature pre-equilibration is effective; post-high-temperature pre-equilibration, the system is in its favored six-coordinate environment, while the trajectory without pre-equilibration passes through CNs ranging from 6.6 to 5.2, before reaching the six-coordinate minimum after over 35 ps of simulation time. Similarly, the BME-MD gradients show no significant changes and oscillate around a consistent mean after only 1.25 ps for the high-temperature, pre-equilibrated trajectory whereas this is only achieved after roughly 31.25 ps in the non-pre-equilibrated simulation (Figure S2). Based on these initial results, all initial configurations generated from slow-growth simulation, utilized for the previously discussed non-pre-equilibrated BME-MD FECs (Figure 3a), were used again as initial configurations and 1.25-ps long trajectories were simulated at 370 K. A new set of 20-ps 300 K trajectories, focusing on the SSHIP to CIP transition, then was started from the final structures of the 370-K simulations. The resulting, successively integrated, 5-ps BME-MD FECs are displayed in Figure 3b, along with the final FEC averaged over 18.25 ps after discarding the first 1.75 ps of each trajectory as pre-equilibration. Inspection of the FECs reveals only minor variation across the successive 5-ps intervals, again suggesting that high-temperature pre-equilibration can alleviate issues arising from slow dehydration dynamics of Mg^{2+} and strong hydration of SO_4^{2-}. Note that the comparatively fast convergence of the BME-MD FEC allowed for a finer R(Mg-S) grid to be simulated, with extra points at 4.125 Å, 4.25 Å, and 4.75 Å added for smoother integration of the BME gradients for the SSHIP-to-η_1-CIP transition.

The final BME-MD FECs, with and without high-temperature pre-equilibration, are compared in Figure 3c, which also displays the Mg-O_w and Mg-O CNs along the RC. As

expected, for the vast majority of sampled R(Mg-S) values, the Mg^{2+} cation remains in a hexacoordinate configuration. This is in agreement with its well-studied hydration dynamics; the Mg^{2+} ion is unable to expand its coordination sphere beyond six, and dehydration is associated with significant free energy barriers.[65, 104-106] The energetics for the SSHIP-to-η_1-CIP transition generally agree between both simulations: high-temperature pre-equilibration yields a barrier of 0.30 eV and a reaction free energy of 0.13 eV, while no pre-equilibration yields a barrier of 0.27 eV and a reaction free energy of 0.15 eV. However, significant differences are apparent for the η_1-CIP to η_2-CIP transition. The FEC obtained without 370-K pre-equilibration yields near-degenerate mono- and bidentate coordination modes for the CIP, separated by a 0.08 eV barrier, predicting a lower barrier for interconversion between CIP coordination modes than for the dissociation back to SSHIPs. Conversely, the post-high-temperature pre-equilibration trajectories result in a FEC revealing the η_2-CIP to be an extremely shallow minimum, lying 0.23 eV above the η_1-CIP. Inspection of the FECs obtained from successive 5-ps intervals from the non-pre-equilibrated simulations (Figure 3a) reveals a trend toward destabilized bidentate CIPs in the later intervals (intervals from 50 ps onwards). This suggests that the stability of the η_2-CIP in the non-pre-equilibrated trajectories may be an artifact of the system being trapped in an unfavorable coordination environment. Comparison of CNs accessed during the monodentate-to-bidentate transition across the two FECs reveals a shift to a later TS after high-temperature pre-equilibration (Figure 3c), resulting in a pathway that passes through ~6.5 coordinate configurations, as opposed to the non-pre-equilibrated trajectories, which pass through ~5.5 coordinate configurations instead. Further inspection of the BME-MD gradients and accessed CNs for the R(Mg-S) = 3.10 Å trajectories corresponding to TS2 (SI Figure S3) shows minimal variation for the pre-equilibrated trajectory, while large oscillations in both gradient and CN are observed across the non-pre-equilibrated trajectory. Importantly, a large jump in both CN and BME-MD gradient are observed in the non-pre-equilibrated trajectory after ~55 ps, after which the system displays similar CN and BME-MD gradients to the pre-equilibrated trajectory.

These observations strongly suggest that the non-pre-equilibrated system is trapped in a local minimum for the first 55 ps of the simulation, which is readily overcome via high-temperature pre-equilibration. As the BME-MD FEC following high-temperature pre-equilibration shows good convergence and no significant changes if integrated over successive 5-

ps periods (Figure 3b), we determine this FEC to be reliable and utilize it for further ECW theory simulations.

3.3. ECW Theory Simulations

Following convergence of the BME-MD FECs, we carried out ECW theory calculations utilizing embedded Møller-Plesset second-order perturbation theory (EMB-MP2) to correct errors in the internal energy component of the free energies arising from approximations to the XC energy in the revPBE functional. Such corrections are critical to capturing accurately the energetics of ion-pairing processes since pure GGA functionals such as revPBE produce spurious charge delocalization, which unphysically lowers the energy of charge-separated systems.[84] In the case of ion-pair formation, this leads to unphysical lowering of the SSIP and SSHIP states with respect to the CIPs. We previously showed that these errors are substantial for the ion-pairing reactions between Mg^{2+} and Ca^{2+} with CO_3^{2-} and demonstrated the ability of EMB-MP2 calculations to yield corrected free energy profiles.[64] That said, we cannot correct for any possible errors in the free energies arising from entropic or configurational artifacts in the underlying revPBE-D3BJ-MD trajectories.

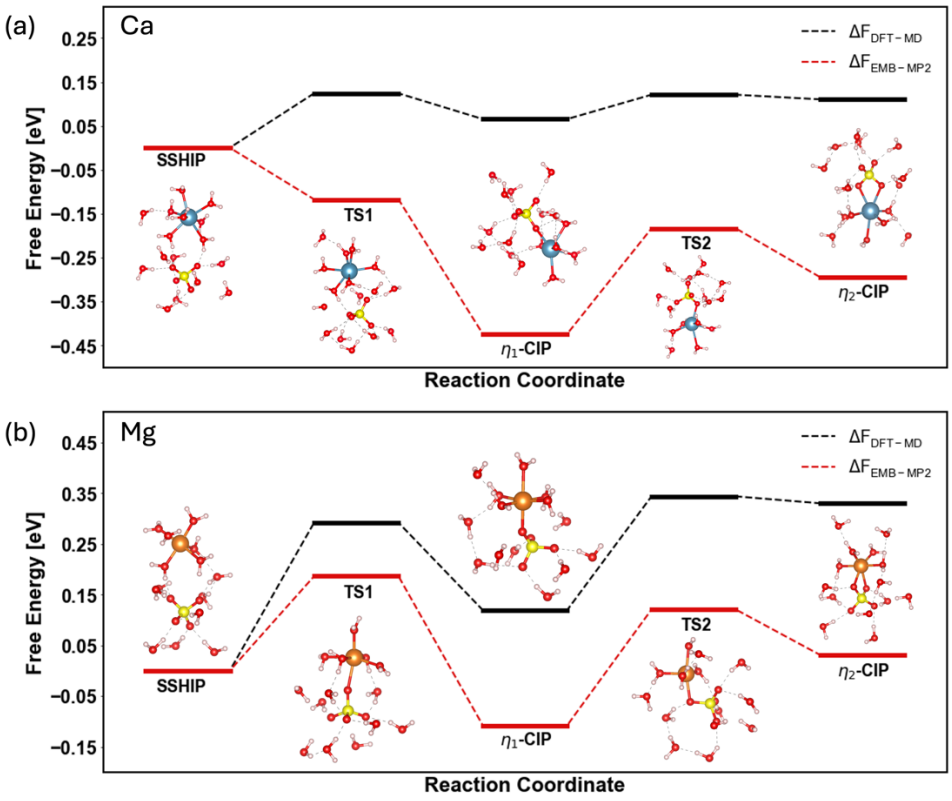

Figure 4. DFT and ECW-corrected free-energy profiles for ion-pair formations of (a): Ca-SO_4, and (b): Mg-SO_4. Black profiles correspond to the BME DFT-MD data, while red profiles show the EMB-MP2-corrected results. Images display a representative geometry of each studied structure, chosen as the final structure from the 20-ps (Ca-SO_4) and 18.25-ps (Mg-SO_4) production BME-constrained MD simulation. Embedded clusters consisted of $Ca(SO_4)(H_2O)_{16}$ and $Mg(SO_4)(H_2O)_{14}$, for the Ca-SO_4 and Mg-SO_4 ion pairing, respectively.

Our embedded cluster here is defined by the reactive species (Mg^{2+}/Ca^{2+} and SO_4^{2-}) in addition to their first coordination shell environment of six and eight waters for Mg^{2+} and Ca^{2+}, respectively, and eight waters for SO_4^{2-}, allowing for the explicit accounting of key solvation and hydrogen-bonding effects along the reaction pathway. The corrected EMB-MP2 free energy profiles are displayed and compared with the uncorrected DFT-revPBE-D3BJ results in Figure 4, which also shows representative structures of the different critical points along the RC. Sizeable corrections to the DFT-revPBE-D3BJ free energies of up to 0.45 eV are obtained for both the Ca and Mg systems and contrasts between the two systems are amplified. The Ca-SO_4 SSHIP to CIP conversion now is predicted to be barrierless and significantly downhill, with the η_1-CIP lying -0.42 eV below the SSHIP. The bidentate coordination mode is predicted to be less favorable than the monodentate mode, lying 0.13 eV above the latter, with a forward barrier of formation of 0.24 eV. In the case of Mg-SO_4, the SSHIP to η_1-CIP reaction is predicted to be favorable by only -0.11 eV and associated with a barrier of 0.19 eV. Similar to Ca-SO_4, the bidentate

configuration lies 0.14 eV above the monodentate one, and the forward barrier to interconversion is 0.23 eV. Experimental dielectric spectroscopy data[107] has suggested the CIP lies 0.06 eV above the SSHIP configuration, however, no distinction between mono- and bi-dentate modes was possible and the measurements are associated with significant uncertainty. Our EMB-MP2 free energy of the bi-dentate coordination mode aligns with the experimentally observed "CIP". Overall, EMB-MP2 yields qualitatively different trends than DFT-revPBE-D3BJ, with Ca-SO_4 ion pairing strongly favorable with no barrier for the former, versus activated and unfavorable for the latter level of theory. For Mg-SO_4, once again EMB-MP2 predicts a very different outcome than DFT-revPBE-D3BJ, with ion pairing favorable for the former versus unfavorable for the latter, showing that even qualitative trends may not be reliable from DFT-MD whenever charged species are involved.

4. Discussion and Conclusions

The new multi-level simulations presented here aid in reducing longstanding uncertainties regarding the relative stability of different ion-pairing modes in $MgSO_4$. Experiments have reached contradictory conclusions, with some studies, e.g., utilizing sound absorption, Raman, and dielectric spectroscopy,[11] suggesting the presence of SSIPs, SSHIPs, and CIPs, whereas dielectric and terahertz absorption spectroscopy[42] indicating the presence of only SSIPs and SSHIPs but no CIPs. Limited simulation data was available to resolve this controversy, with classical FF-MD,[42, 47] QM/MM,[39] and DFT (BLYP)[51] largely focused on reproducing dielectric spectra rather than evaluating ion-pairing energetics. The sole reported MD-derived potential of mean force relied on AMBER FFs,[108] which showed the η_1-CIP to lie slightly below the SSHIP, with a TS1 barrier of ~0.28 eV, in qualitative agreement with our EMB-MP2 results. However, AMBER-FF-MD predicted the bi- and tri-dentate configurations to be degenerate, and more favorable than the monodentate configuration.[52] By contrast, we predict the η_2-CIP to have only a shallow minimum lying significantly above the η_1-CIP, and are unable to resolve a stationary point for a tridentate configuration. This discrepancy likely is due to the difficulty classical FFs inherently have in describing the interplay between (classical) ionic and (QM) dative bonding across the different Mg-SO_4 CIPs, or due to general sampling issues in the strongly hydrated Mg-SO_4 system (note that the earlier study utilized 1D umbrella sampling which, unlike the BME-MD here, may not readily sample orthogonal coordinates).

Our EMB-MP2 results, however, provide further evidence for the existence of CIPs in aqueous Mg-SO_4 solutions. Further, they provide new benchmarking data for the interactions of strongly solvated Mg^{2+} and SO_4^{2-} ions in aqueous solution, illustrating the importance of a balanced treatment of solvation, electrostatic, and electron exchange-correlation effects. The Mg-SO_4 results presented here also emphasize the difficulty of accurately characterizing the free energetics of such strongly solvated systems on the limited timescales accessible for AIMD. However, we do demonstrate that constrained BME-MD is a viable method to elucidate the energetics of such systems, even if all degrees of freedom cannot be actively sampled, by instead utilizing high-temperature pre-equilibration to relax orthogonal degrees of freedom and find the minimum pathway along the FEC.

Previously reported FECs for Ca-SO_4 ion pairing have relied on classical FFs or DFT-BLYP-D3, another semi-local GGA functional suffering from charge delocalization errors.[57] Interestingly, while our DFT-revPBE-D3BJ simulations here agree well with the earlier DFT-BLYP-D3 results, none of the published FF-MD data[57] mirror the predictions obtained with EMB-MP2. Although AMOEBA-MD[109] simulations, which agreed with EMB-MP2 for Ca/Mg-CO_3 ion-pairing,[64, 110] show some stabilization of the CIP compared to DFT-MD, the CIP was still predicted to lie marginally higher than the SSHIP. By contrast, our multi-level EMB-MP2 simulations predict CIPs to be the preferred coordination environment for Ca-SO_4 in concentrated aqueous environments. We do note that the predicted free energy of formation for the CIPs from our EMB-MP2 simulations is significantly more exergonic than those previously reported. The magnitude of our EMB-MP2 correction is in line with those found previously for, e.g., Mg-CO_3 ion-pairing, which agreed with previously reported simulations.[64] We conclude that further investigation into the source of this disagreement is warranted, e.g., via the use of machine-learned FFs,[111] which may correct possible errors arising from entropic factors and allow for simulation of larger cells, enabling direct comparison with experimental standard free energies of ion pairing.

In summary, the results presented in this study shine new light on pre-nucleation processes in concentrated $MgSO_4$ and $CaSO_4$ solutions, obtaining ab-initio FECs for initial ion-pairing reactions. For $CaSO_4$, formation of a CIP is predicted to be an extremely favorable, exergonic process with no barrier, while for $MgSO_4$, CIP formation is only slightly exergonic and associated with a non-negligible barrier. While we have only considered pre-nucleation behavior and not solid dissolution/precipitation, and therefore cannot directly relate these trends to solubilities, these

differences are qualitatively consistent with the observed differences in solubility for the two different sulfate minerals: $CaSO_4$ exhibits an extremely low solubility in water, while $MgSO_4$ dissolves readily. This low solubility of $CaSO_4$ correlates with the highly exergonic ion association calculated in this work, making dissolution of close-contact Ca-SO_4 pairs a process associated with a high energetic penalty in water. This behavior is not observed for $MgSO_4$, consistent with its higher solubility.

ASSOCIATED CONTENT

Supporting Information.

The following files are available free of charge.

BME-MD FEC convergence, BME gradient and CN convergence at TS1 and TS2 (PDF)

DATA AVAILABILITY STATEMENT

The data that supports the findings of this study are available within the article [and its supplementary material].

AUTHOR INFORMATION

Corresponding Author

*eac@princeton.edu

Author Contributions

The manuscript was written through contributions of both authors. Both authors have given approval to the final version of the manuscript.

ACKNOWLEDGMENT

This work was conducted within the Computational Chemical Science Center: Chemistry in Solution and at Interfaces at Princeton University, supported as part of the Computational Chemical Sciences Program funded by the U.S. Department of Energy (DoE), Office of Science, Basic Energy Sciences, under Award No. DE-SC0019394. We additionally thank the Princeton Catalysis Initiative for providing supplementary funding for this work.

References

(1) Millero, F. J.; Feistel, R.; Wright, D. G.; McDougall, T. J. The composition of Standard Seawater and the definition of the Reference-Composition Salinity Scale. *Deep Sea Res. Part I Oceanogr. Res. Pap.* **2008**, *55* (1), 50-72.
(2) Thomas, M. V.; Puleo, D. A. Calcium sulfate: Properties and clinical applications. *Journal of Biomedical Materials Research Part B: Applied Biomaterials* **2009**, *88B* (2), 597-610. DOI: https://doi.org/10.1002/jbm.b.31269 (acccessed 2024/07/24).
(3) García-Maté, M.; De la Torre, A. G.; León-Reina, L.; Losilla, E. R.; Aranda, M. A. G.; Santacruz, I. Effect of calcium sulfate source on the hydration of calcium sulfoaluminate eco-cement. *Cement and Concrete Composites* **2015**, *55*, 53-61. DOI: https://doi.org/10.1016/j.cemconcomp.2014.08.003.
(4) Karni, J.; Karni, E. Y. Gypsum in construction: origin and properties. *Materials and Structures* **1995**, *28* (2), 92-100. DOI: 10.1007/BF02473176.
(5) Charola, A. E.; Pühringer, J.; Steiger, M. Gypsum: a review of its role in the deterioration of building materials. *Environmental Geology* **2007**, *52* (2), 339-352. DOI: 10.1007/s00254-006-0566-9.
(6) Palacio, S.; Escudero, A.; Montserrat-Martí, G.; Maestro, M.; Milla, R.; Albert, M. J. Plants Living on Gypsum: Beyond the Specialist Model. *Annals of Botany* **2007**, *99* (2), 333-343. DOI: 10.1093/aob/mcl263 (acccessed 7/25/2024).
(7) Moghadasi, J.; Jamialahmadi, M.; Müller-Steinhagen, H.; Sharif, A. Scale Formation in Oil Reservoir and Production Equipment during Water Injection Kinetics of $CaSO_4$ and $CaCO_3$ Crystal Growth and Effect on Formation Damage. In SPE European Formation Damage Conference, 2003.
(8) Shen, J.; Crosby, C. C. Insight Into Strontium and Calcium Sulfate Scaling Mechanisms in a Wet Producer. *Journal of Petroleum Technology* **1983**, *35* (07), 1249-1255. DOI: 10.2118/10597-PA (acccessed 7/25/2024).
(9) Le Gouellec, Y. A.; Elimelech, M. Calcium sulfate (gypsum) scaling in nanofiltration of agricultural drainage water. *Journal of Membrane Science* **2002**, *205* (1), 279-291. DOI: https://doi.org/10.1016/S0376-7388(02)00128-X.
(10) Hasson, D.; Zahavi, J. Mechanism of Calcium Sulfate Scale Deposition on Heat Transfer Surfaces. *Industrial & Engineering Chemistry Fundamentals* **1970**, *9* (1), 1-10. DOI: 10.1021/i160033a001.
(11) Buchner, R.; Chen, T.; Hefter, G. Complexity in "Simple" Electrolyte Solutions: Ion Pairing in $MgSO_4$(aq). *The Journal of Physical Chemistry B* **2004**, *108* (7), 2365-2375. DOI: 10.1021/jp034870p.
(12) van Dam, R. A.; Hogan, A. C.; McCullough, C. D.; Houston, M. A.; Humphrey, C. L.; Harford, A. J. Aquatic toxicity of magnesium sulfate, and the influence of calcium, in very low ionic concentration water. *Environmental Toxicology and Chemistry* **2010**, *29* (2), 410-421. DOI: https://doi.org/10.1002/etc.56 (acccessed 2024/07/24).
(13) Vaniman, D. T.; Bish, D. L.; Chipera, S. J.; Fialips, C. I.; William Carey, J.; Feldman, W. C. Magnesium sulphate salts and the history of water on Mars. *Nature* **2004**, *431* (7009), 663-665. DOI: 10.1038/nature02973.
(14) Zolotov, M. Y.; Shock, E. L. Composition and stability of salts on the surface of Europa and their oceanic origin. *Journal of Geophysical Research: Planets* **2001**, *106* (E12), 32815-32827. DOI: https://doi.org/10.1029/2000JE001413 (acccessed 2024/07/25).

(15) Stawski, T. M.; Van Driessche, A. E. S.; Besselink, R.; Byrne, E. H.; Raiteri, P.; Gale, J. D.; Benning, L. G. The Structure of $CaSO_4$ Nanorods: The Precursor of Gypsum. *The Journal of Physical Chemistry C* **2019**, *123* (37), 23151-23158. DOI: 10.1021/acs.jpcc.9b04268.
(16) Stawski, T. M.; Freeman, H. M.; Van Driessche, A. E. S.; Hövelmann, J.; Besselink, R.; Wirth, R.; Benning, L. G. Particle-Mediated Nucleation Pathways Are Imprinted in the Internal Structure of Calcium Sulfate Single Crystals. *Crystal Growth & Design* **2019**, *19* (7), 3714-3721. DOI: 10.1021/acs.cgd.9b00066.
(17) Tritschler, U.; Kellermeier, M.; Debus, C.; Kempter, A.; Cölfen, H. A simple strategy for the synthesis of well-defined bassanite nanorods. *CrystEngComm* **2015**, *17* (20), 3772-3776, 10.1039/C5CE00519A. DOI: 10.1039/C5CE00519A.
(18) Tritschler, U.; Van Driessche, A. E. S.; Kempter, A.; Kellermeier, M.; Cölfen, H. Controlling the Selective Formation of Calcium Sulfate Polymorphs at Room Temperature. *Angewandte Chemie International Edition* **2015**, *54* (13), 4083-4086. DOI: https://doi.org/10.1002/anie.201409651 (acccessed 2024/09/17).
(19) Mehta, P. K. Mechanism of sulfate attack on portland cement concrete — Another look. *Cement and Concrete Research* **1983**, *13* (3), 401-406. DOI: https://doi.org/10.1016/0008-8846(83)90040-6.
(20) Tikalsky, P. J.; Roy, D.; Scheetz, B.; Krize, T. Redefining cement characteristics for sulfate-resistant Portland cement. *Cement and Concrete Research* **2002**, *32* (8), 1239-1246. DOI: https://doi.org/10.1016/S0008-8846(02)00767-6.
(21) Cardell, C.; Benavente, D.; Rodríguez-Gordillo, J. Weathering of limestone building material by mixed sulfate solutions. Characterization of stone microstructure, reaction products and decay forms. *Materials Characterization* **2008**, *59* (10), 1371-1385. DOI: https://doi.org/10.1016/j.matchar.2007.12.003.
(22) Wu, Q.; Xue, Q.; Yu, Z. Research status of super sulfate cement. *Journal of Cleaner Production* **2021**, *294*, 126228. DOI: https://doi.org/10.1016/j.jclepro.2021.126228.
(23) Flatt, R. J.; Roussel, N.; Cheeseman, C. R. Concrete: An eco material that needs to be improved. *Journal of the European Ceramic Society* **2012**, *32* (11), 2787-2798. DOI: https://doi.org/10.1016/j.jeurceramsoc.2011.11.012.
(24) Lehne, J.; Preston, F. *Making Concrete Change. Innovation in Low-carbon Cement and Concrete*; Energy, Environment, and Resources Department, 2018.
(25) Fernández-Díaz, L.; Fernández-González, Á.; Prieto, M. The role of sulfate groups in controlling $CaCO_3$ polymorphism. *Geochimica et Cosmochimica Acta* **2010**, *74* (21), 6064-6076. DOI: https://doi.org/10.1016/j.gca.2010.08.010.
(26) Ihli, J.; Kim, Y.-Y.; Noel, E. H.; Meldrum, F. C. The Effect of Additives on Amorphous Calcium Carbonate (ACC): Janus Behavior in Solution and the Solid State. *Advanced Functional Materials* **2013**, *23* (12), 1575-1585. DOI: https://doi.org/10.1002/adfm.201201805 (acccessed 2024/07/24).
(27) Chang, R.; Kim, S.; Lee, S.; Choi, S.; Kim, M.; Park, Y. Calcium carbonate precipitation for CO2 storage and utilization: a review of the carbonate crystallization and polymorphism. *Front. Energy Res.* **2017**, *5*, 17.
(28) Hills, C. D.; Tripathi, N.; Carey, P. J. Mineralization Technology for Carbon Capture, Utilization, and Storage. *Front. Energy Res.* **2020**, *8*, Review. DOI: 10.3389/fenrg.2020.00142.
(29) Lackner, K. S.; Wendt, C. H.; Butt, D. P.; Joyce, E. L.; Sharp, D. H. Carbon dioxide disposal in carbonate minerals. *Energy* **1995**, *20* (11), 1153-1170. DOI: https://doi.org/10.1016/0360-5442(95)00071-N.

(30) Matter, J. M.; Stute, M.; Snæbjörnsdottir, S. Ó.; Oelkers, E. H.; Gislason, S. R.; Aradottir, E. S.; Sigfusson, B.; Gunnarsson, I.; Sigurdardottir, H.; Gunnlaugsson, E.; et al. Rapid carbon mineralization for permanent disposal of anthropogenic carbon dioxide emissions. *Science* **2016**, *352* (6291), 1312-1314. DOI: doi:10.1126/science.aad8132.
(31) Romanov, V.; Soong, Y.; Carney, C.; Rush, G. E.; Nielsen, B.; O'Connor, W. Mineralization of Carbon Dioxide: A Literature Review. *ChemBioEng Reviews* **2015**, *2* (4), 231-256. DOI: https://doi.org/10.1002/cben.201500002.
(32) La Plante, E. C.; Chen, X.; Bustillos, S.; Bouissonnie, A.; Traynor, T.; Jassby, D.; Corsini, L.; Simonetti, D. A.; Sant, G. N. Electrolytic Seawater Mineralization and the Mass Balances That Demonstrate Carbon Dioxide Removal. *ACS ES&T Engineering* **2023**, *3* (7), 955-968. DOI: 10.1021/acsestengg.3c00004.
(33) Rigopoulos, I.; Harrison, A. L.; Delimitis, A.; Ioannou, I.; Efstathiou, A. M.; Kyratsi, T.; Oelkers, E. H. Carbon sequestration via enhanced weathering of peridotites and basalts in seawater. *Appl. Geochem.* **2018**, *91*, 197-207.
(34) Sharifian, R.; Boer, L.; Wagterveld, R. M.; Vermaas, D. A. Oceanic carbon capture through electrochemically induced in situ carbonate mineralization using bipolar membrane. *Chemical Engineering Journal* **2022**, *438*, 135326. DOI: https://doi.org/10.1016/j.cej.2022.135326.
(35) Zhao, Y.; Wang, J.; Ji, Z.; Liu, J.; Guo, X.; Yuan, J. A novel technology of carbon dioxide adsorption and mineralization via seawater decalcification by bipolar membrane electrodialysis system with a crystallizer. *Chem. Eng. J.* **2020**, *381*, 122542.
(36) La Plante, E. C.; Simonetti, D. A.; Wang, J.; Al-Turki, A.; Chen, X.; Jassby, D.; Sant, G. N. Saline water-based mineralization pathway for gigatonne-scale CO_2 management. *ACS Sustain. Chem. Eng.* **2021**, *9* (3), 1073-1089.
(37) Li, Y.; Zeng, H.; Zhang, H. Atomistic simulations of nucleation and growth of $CaCO_3$ with the influence of inhibitors: A review. *Materials Genome Engineering Advances* **2023**, *1* (1), e4. DOI: https://doi.org/10.1002/mgea.4 (acccessed 2024/07/24).
(38) Caminiti, R. Any x-ray diffraction study on SO_4^{2-}-H2O interactions in the presence of nickel and magnesium ions. *Chemical Physics Letters* **1982**, *88* (1), 103-108. DOI: https://doi.org/10.1016/0009-2614(82)80079-1.
(39) Kundu, A.; Mamatkulov, S. I.; Brünig, F. N.; Bonthuis, D. J.; Netz, R. R.; Elsaesser, T.; Fingerhut, B. P. Short-Range Cooperative Slow-down of Water Solvation Dynamics Around SO_4^{2-}–Mg^{2+} Ion Pairs. *ACS Physical Chemistry Au* **2022**, *2* (6), 506-514. DOI: 10.1021/acsphyschemau.2c00034.
(40) Rudolph, W. W.; Irmer, G.; Hefter, G. T. Raman spectroscopic investigation of speciation in $MgSO_4$(aq). *Physical Chemistry Chemical Physics* **2003**, *5* (23), 5253-5261, 10.1039/B308951G. DOI: 10.1039/B308951G.
(41) Rull, F.; Balarew, C.; Alvarez, J. L.; Sobron, F.; Rodriguez, A. Raman spectroscopic study of ion association in aqueous magnesium sulphate solutions. *Journal of Raman Spectroscopy* **1994**, *25* (12), 933-941. DOI: https://doi.org/10.1002/jrs.1250251206.
(42) Sebastiani, F.; Verde, A. V.; Heyden, M.; Schwaab, G.; Havenith, M. Cooperativity and ion pairing in magnesium sulfate aqueous solutions from the dilute regime to the solubility limit. *Physical Chemistry Chemical Physics* **2020**, *22* (21), 12140-12153, 10.1039/C9CP06845G. DOI: 10.1039/C9CP06845G.
(43) Daly, F. P.; Brown, C. W.; Kester, D. R. Sodium and magnesium sulfate ion pairing. Evidence from Raman spectroscopy. *The Journal of Physical Chemistry* **1972**, *76* (24), 3664-3668. DOI: 10.1021/j100668a027.

(44) Davis, A. R.; Oliver, B. G. Raman spectroscopic evidence for contact ion pairing in aqueous magnesium sulfate solutions. *The Journal of Physical Chemistry* **1973**, *77* (10), 1315-1316. DOI: 10.1021/j100629a028.
(45) Götte, L.; Parry, K. M.; Hua, W.; Verreault, D.; Allen, H. C.; Tobias, D. J. Solvent-Shared Ion Pairs at the Air–Solution Interface of Magnesium Chloride and Sulfate Solutions Revealed by Sum Frequency Spectroscopy and Molecular Dynamics Simulations. *The Journal of Physical Chemistry A* **2017**, *121* (34), 6450-6459. DOI: 10.1021/acs.jpca.7b05600.
(46) Tielrooij, K. J.; Garcia-Araez, N.; Bonn, M.; Bakker, H. J. Cooperativity in Ion Hydration. *Science* **2010**, *328* (5981), 1006-1009. DOI: 10.1126/science.1183512 (acccessed 2024/07/24).
(47) Mamatkulov, S. I.; Rinne, K. F.; Buchner, R.; Netz, R. R.; Bonthuis, D. J. Water-separated ion pairs cause the slow dielectric mode of magnesium sulfate solutions. *The Journal of Chemical Physics* **2018**, *148* (22), 222812. DOI: 10.1063/1.5000385 (acccessed 7/22/2024).
(48) Vila Verde, A.; Santer, M.; Lipowsky, R. Solvent-shared pairs of densely charged ions induce intense but short-range supra-additive slowdown of water rotation. *Physical Chemistry Chemical Physics* **2016**, *18* (3), 1918-1930, 10.1039/C5CP05726D. DOI: 10.1039/C5CP05726D.
(49) Vila Verde, A.; Lipowsky, R. Cooperative Slowdown of Water Rotation near Densely Charged Ions Is Intense but Short-Ranged. *The Journal of Physical Chemistry B* **2013**, *117* (36), 10556-10566. DOI: 10.1021/jp4059802.
(50) Balasubramanian, G.; Murad, S.; Kappiyoor, R.; Puri, I. K. Structure of aqueous $MgSO_4$ solution: Dilute to concentrated. *Chemical Physics Letters* **2011**, *508* (1), 38-42. DOI: https://doi.org/10.1016/j.cplett.2011.04.010.
(51) Jahn, S.; Schmidt, C. Speciation in Aqueous $MgSO_4$ Fluids at High Pressures and High Temperatures from ab Initio Molecular Dynamics and Raman Spectroscopy. *The Journal of Physical Chemistry B* **2010**, *114* (47), 15565-15572. DOI: 10.1021/jp101749h.
(52) Duvail, M.; Villard, A.; Nguyen, T.-N.; Dufrêche, J.-F. Thermodynamics of Associated Electrolytes in Water: Molecular Dynamics Simulations of Sulfate Solutions. *The Journal of Physical Chemistry B* **2015**, *119* (34), 11184-11195. DOI: 10.1021/acs.jpcb.5b03088.
(53) Stawski, T. M.; van Driessche, A. E. S.; Ossorio, M.; Diego Rodriguez-Blanco, J.; Besselink, R.; Benning, L. G. Formation of calcium sulfate through the aggregation of sub-3 nanometre primary species. *Nature Communications* **2016**, *7* (1), 11177. DOI: 10.1038/ncomms11177.
(54) Jones, F. Infrared investigation of barite and gypsum crystallization: Evidence for an amorphous to crystalline transition. *CrystEngComm* **2012**, *14* (24), 8374-8381, 10.1039/C2CE25918D. DOI: 10.1039/C2CE25918D.
(55) Saha, A.; Lee, J.; Pancera, S. M.; Bräeu, M. F.; Kempter, A.; Tripathi, A.; Bose, A. New Insights into the Transformation of Calcium Sulfate Hemihydrate to Gypsum Using Time-Resolved Cryogenic Transmission Electron Microscopy. *Langmuir* **2012**, *28* (30), 11182-11187. DOI: 10.1021/la3024474.
(56) Wang, Y.-W.; Kim, Y.-Y.; Christenson, H. K.; Meldrum, F. C. A new precipitation pathway for calcium sulfate dihydrate (gypsum) via amorphous and hemihydrate intermediates. *Chemical Communications* **2012**, *48* (4), 504-506, 10.1039/C1CC14210K. DOI: 10.1039/C1CC14210K.
(57) Byrne, E. H.; Raiteri, P.; Gale, J. D. Computational Insight into Calcium–Sulfate Ion Pair Formation. *The Journal of Physical Chemistry C* **2017**, *121* (46), 25956-25966. DOI: 10.1021/acs.jpcc.7b09820.

(58) Huang, C.; Pavone, M.; Carter, E. A. Quantum mechanical embedding theory based on a unique embedding potential. *The Journal of Chemical Physics* **2011**, *134* (15). DOI: 10.1063/1.3577516 (acccessed 2/21/2024).
(59) Libisch, F.; Huang, C.; Carter, E. A. Embedded Correlated Wavefunction Schemes: Theory and Applications. *Acc. Chem. Res.* **2014**, *47* (9), 2768-2775. DOI: 10.1021/ar500086h.
(60) Yu, K.; Krauter, C. M.; Dieterich, J. M.; Carter, E. A. Density and Potential Functional Embedding: Theory and Practice. In *Fragmentation: Toward Accurate Calculations on Complex Molecular Systems*, Mark Gordon, Ed. (John Wiley & Sons), 2017; pp 81-117.
(61) Yu, K.; Libisch, F.; Carter, E. A. Implementation of density functional embedding theory within the projector-augmented-wave method and applications to semiconductor defect states. *The Journal of Chemical Physics* **2015**, *143* (10). DOI: 10.1063/1.4922260 (acccessed 2/21/2024).
(62) Kellermeier, M.; Raiteri, P.; Berg, J. K.; Kempter, A.; Gale, J. D.; Gebauer, D. Entropy Drives Calcium Carbonate Ion Association. *ChemPhysChem* **2016**, *17* (21), 3535-3541. DOI: https://doi.org/10.1002/cphc.201600653.
(63) Martirez, J. M. P.; Carter, E. A. Solvent Dynamics Are Critical to Understanding Carbon Dioxide Dissolution and Hydration in Water. *Journal of the American Chemical Society* **2023**, *145* (23), 12561-12575. DOI: 10.1021/jacs.3c01283.
(64) Boyn, J.-N.; Carter, E. A. Characterizing the Mechanisms of Ca and Mg Carbonate Ion-Pair Formation with Multi-Level Molecular Dynamics/Quantum Mechanics Simulations. *The Journal of Physical Chemistry B* **2023**, *127* (50), 10824-10832. DOI: 10.1021/acs.jpcb.3c05369.
(65) Boyn, J.-N.; Carter, E. A. Probing pH-Dependent Dehydration Dynamics of Mg and Ca Cations in Aqueous Solutions with Multi-Level Quantum Mechanics/Molecular Dynamics Simulations. *Journal of the American Chemical Society* **2023**, *145* (37), 20462-20472. DOI: 10.1021/jacs.3c06182.
(66) Gebauer, D.; Kellermeier, M.; Gale, J. D.; Bergström, L.; Cölfen, H. Pre-nucleation clusters as solute precursors in crystallisation. *Chem. Soc. Rev.* **2014**, *43* (7), 2348-2371.
(67) Gebauer, D.; Wolf, S. E. Designing Solid Materials from Their Solute State: A Shift in Paradigms toward a Holistic Approach in Functional Materials Chemistry. *Journal of the American Chemical Society* **2019**, *141* (11), 4490-4504. DOI: 10.1021/jacs.8b13231.
(68) Henzler, K.; Fetisov, E. O.; Galib, M.; Baer, M. D.; Legg, B. A.; Borca, C.; Xto, J. M.; Pin, S.; Fulton, J. L.; Schenter, G. K.; et al. Supersaturated calcium carbonate solutions are classical. *Science Advances* **2018**, *4* (1), eaao6283. DOI: doi:10.1126/sciadv.aao6283.
(69) Zeron, I. M.; Abascal, J. L. F.; Vega, C. A force field of Li^+, Na^+, K^+, Mg^{2+}, Ca^{2+}, Cl^-, and SO_4^{2-} in aqueous solution based on the TIP4P/2005 water model and scaled charges for the ions. *The Journal of Chemical Physics* **2019**, *151* (13), 134504. DOI: 10.1063/1.5121392 (acccessed 7/24/2024).
(70) Kresse, G.; Furthmüller, J. Efficiency of ab-initio total energy calculations for metals and semiconductors using a plane-wave basis set. *Comput. Mater. Sci.* **1996**, *6* (1), 15-50.
(71) Kresse, G.; Furthmüller, J. Efficient iterative schemes for ab initio total-energy calculations using a plane-wave basis set. *Phys. Rev. B* **1996**, *54* (16), 11169.
(72) Kresse, G.; Joubert, D. From ultrasoft pseudopotentials to the projector augmented-wave method. *Phys. Rev. B* **1999**, *59* (3), 1758.
(73) Zhang, Y.; Yang, W. Comment on "Generalized gradient approximation made simple". *Phys. Rev. Lett.* **1998**, *80* (4), 890.

(74) Grimme, S.; Antony, J.; Ehrlich, S.; Krieg, H. A consistent and accurate ab initio parametrization of density functional dispersion correction (DFT-D) for the 94 elements H-Pu. *J. Chem. Phys.* **2010**, *132* (15), 154104.
(75) Grimme, S.; Ehrlich, S.; Goerigk, L. Effect of the damping function in dispersion corrected density functional theory. *J. Comput. Chem.* **2011**, *32* (7), 1456-1465.
(76) Ruiz Pestana, L.; Mardirossian, N.; Head-Gordon, M.; Head-Gordon, T. Ab initio molecular dynamics simulations of liquid water using high quality meta-GGA functionals. *Chem. Sci.* **2017**, *8* (5), 3554-3565, 10.1039/C6SC04711D. DOI: 10.1039/C6SC04711D.
(77) Blöchl, P. E. Projector augmented-wave method. *Physical Review B* **1994**, *50* (24), 17953-17979. DOI: 10.1103/PhysRevB.50.17953.
(78) Evans, D. J.; Holian, B. L. The nose–hoover thermostat. *J. Chem. Phys.* **1985**, *83* (8), 4069-4074.
(79) Nosé, S. A unified formulation of the constant temperature molecular dynamics methods. *J. Chem. Phys.* **1984**, *81* (1), 511-519. DOI: 10.1063/1.447334.
(80) Carter, E. A.; Ciccotti, G.; Hynes, J. T.; Kapral, R. Constrained reaction coordinate dynamics for the simulation of rare events. *Chem. Phys. Lett.* **1989**, *156* (5), 472-477. DOI: https://doi.org/10.1016/S0009-2614(89)87314-2.
(81) Ryckaert, J.-P.; Ciccotti, G.; Berendsen, H. J. C. Numerical integration of the cartesian equations of motion of a system with constraints: molecular dynamics of n-alkanes. *Journal of Computational Physics* **1977**, *23* (3), 327-341. DOI: https://doi.org/10.1016/0021-9991(77)90098-5.
(82) Virtanen, P.; Gommers, R.; Oliphant, T. E.; Haberland, M.; Reddy, T.; Cournapeau, D.; Burovski, E.; Peterson, P.; Weckesser, W.; Bright, J.; et al. SciPy 1.0: fundamental algorithms for scientific computing in Python. *Nature Methods* **2020**, *17* (3), 261-272. DOI: 10.1038/s41592-019-0686-2.
(83) Oberhofer, H.; Dellago, C.; Geissler, P. L. Biased Sampling of Nonequilibrium Trajectories: Can Fast Switching Simulations Outperform Conventional Free Energy Calculation Methods? *J. Phys. Chem. B* **2005**, *109* (14), 6902-6915. DOI: 10.1021/jp044556a.
(84) Bryenton, K. R.; Adeleke, A. A.; Dale, S. G.; Johnson, E. R. Delocalization error: The greatest outstanding challenge in density-functional theory. *WIREs Computational Molecular Science* **2023**, *13* (2), e1631. DOI: https://doi.org/10.1002/wcms.1631.
(85) Kuang, Y.; Libisch, F.; Carter, E. A.*VASPEmbedding*; https://github.com/EACcodes/VASPEmbedding (accessed 08/26/2024)
(86) Krauter, C. M.; Zhang, X.; Carter, E. A. *EmbeddingIntegralGenerator*; https://github.com/EACcodes/EmbeddingIntegralGenerator (accessed 08/26/2024)
(87) Head-Gordon, M.; Pople, J. A.; Frisch, M. J. MP2 energy evaluation by direct methods. *Chem. Phys. Lett.* **1988**, *153* (6), 503-506. DOI: https://doi.org/10.1016/0009-2614(88)85250-3.
(88) Møller, C.; Plesset, M. S. Note on an Approximation Treatment for Many-Electron Systems. *Physical Review* **1934**, *46* (7), 618-622. DOI: 10.1103/PhysRev.46.618.
(89) Weigend, F.; Ahlrichs, R. Balanced basis sets of split valence, triple zeta valence and quadruple zeta valence quality for H to Rn: Design and assessment of accuracy. *Phys. Chem. Chem. Phys.* **2005**, *7* (18), 3297-3305, 10.1039/B508541A. DOI: 10.1039/B508541A.
(90) Werner, H.-J.; Knowles, P. J.; Manby, F. R.; Black, J. A.; Doll, K.; Heßelmann, A.; Kats, D.; Köhn, A.; Korona, T.; Kreplin, D. A.; et al. The Molpro quantum chemistry package. *J. Chem. Phys.* **2020**, *152* (14), 144107. DOI: 10.1063/5.0005081.

(91) Bleuzen, A.; Pittet, P.-A.; Helm, L.; Merbach, A. E. Water exchange on magnesium(II) in aqueous solution: a variable temperature and pressure ^{17}O NMR study. *Magn. Reson. Chem.* **1997**, *35* (11), 765-773. DOI: https://doi.org/10.1002/(SICI)1097-458X(199711)35:11<765::AID-OMR169>3.0.CO;2-F.
(92) Schwierz, N. Kinetic pathways of water exchange in the first hydration shell of magnesium. *J. Chem. Phys.* **2020**, *152* (22), 224106. DOI: 10.1063/1.5144258.
(93) Falkner, S.; Schwierz, N. Kinetic pathways of water exchange in the first hydration shell of magnesium: Influence of water model and ionic force field. *J. Chem. Phys.* **2021**, *155* (8), 084503. DOI: 10.1063/5.0060896.
(94) Marcus, Y. Effect of Ions on the Structure of Water: Structure Making and Breaking. *Chemical Reviews* **2009**, *109* (3), 1346-1370. DOI: 10.1021/cr8003828.
(95) Iannuzzi, M.; Laio, A.; Parrinello, M. Efficient Exploration of Reactive Potential Energy Surfaces Using Car-Parrinello Molecular Dynamics. *Physical Review Letters* **2003**, *90* (23), 238302. DOI: 10.1103/PhysRevLett.90.238302.
(96) Marcus, Y. Ionic radii in aqueous solutions. *Chem. Rev.* **1988**, *88* (8), 1475-1498.
(97) Ohtaki, H.; Radnai, T. Structure and dynamics of hydrated ions. *Chem. Rev.* **1993**, *93* (3), 1157-1204.
(98) Caminiti, R.; Paschina, G.; Pinna, G.; Magini, M. Experimental evidence of interactions SO_4^{2-} $-H_2O$ in an aqueous solution. *Chemical Physics Letters* **1979**, *64* (2), 391-395. DOI: https://doi.org/10.1016/0009-2614(79)80539-4.
(99) Caminiti, R.; Paschina, G. An X-ray diffraction study of the structure of the aqua indium(III) ion in indium sulphate solution. *Chemical Physics Letters* **1981**, *82* (3), 487-491. DOI: https://doi.org/10.1016/0009-2614(81)85425-5.
(100) Caminiti, R. Complex formation and SO_4^{2-}-H_2O interactions in a concentrated aqueous $Cr_2(SO_4)_3$ solution. *Chemical Physics Letters* **1982**, *86* (2), 214-218. DOI: https://doi.org/10.1016/0009-2614(82)83272-7.
(101) Caminiti, R. Sulphate-H_2O interactions in a concentrated aqueous H2SO4 solution. *Chemical Physics Letters* **1983**, *96* (3), 390-394. DOI: https://doi.org/10.1016/0009-2614(83)80696-4.
(102) Vchirawongkwin, V.; Rode, B. M.; Persson, I. Structure and Dynamics of Sulfate Ion in Aqueous Solution An ab initio QMCF MD Simulation and Large Angle X-ray Scattering Study. *The Journal of Physical Chemistry B* **2007**, *111* (16), 4150-4155. DOI: 10.1021/jp0702402.
(103) Cannon, W. R.; Pettitt, B. M.; McCammon, J. A. Sulfate Anion in Water: Model Structural, Thermodynamic, and Dynamic Properties. *The Journal of Physical Chemistry* **1994**, *98* (24), 6225-6230. DOI: 10.1021/j100075a027.
(104) Aufort, J.; Raiteri, P.; Gale, J. D. Computational Insights into Mg^{2+} Dehydration in the Presence of Carbonate. *ACS Earth Space Chem.* **2022**, *6* (3), 733-745.
(105) Toroz, D.; Song, F.; Uddin, A.; Chass, G. A.; Di Tommaso, D. A Database of Solution Additives Promoting Mg^{2+} Dehydration and the Onset of $MgCO_3$ Nucleation. *Cryst. Growth Des.* **2022**, *22* (5), 3080-3089. DOI: 10.1021/acs.cgd.1c01525.
(106) Zhang, X.; Alvarez-Lloret, P.; Chass, G.; Di Tommaso, D. Interatomic potentials of Mg ions in aqueous solutions: structure and dehydration kinetics. *Eur. J. Mineral.* **2019**, *31* (2), 275-287.
(107) Akilan, C.; Rohman, N.; Hefter, G.; Buchner, R. Temperature Effects on Ion Association and Hydration in $MgSO_4$ by Dielectric Spectroscopy. *ChemPhysChem* **2006**, *7* (11), 2319-2330. DOI: https://doi.org/10.1002/cphc.200600342 (acccessed 2024/09/17).

(108) Case, D. A.; Cheatham Iii, T. E.; Darden, T.; Gohlke, H.; Luo, R.; Merz Jr, K. M.; Onufriev, A.; Simmerling, C.; Wang, B.; Woods, R. J. The Amber biomolecular simulation programs. *Journal of Computational Chemistry* **2005**, *26* (16), 1668-1688. DOI: https://doi.org/10.1002/jcc.20290 (acccessed 2024/07/29).
(109) Ponder, J. W.; Wu, C.; Ren, P.; Pande, V. S.; Chodera, J. D.; Schnieders, M. J.; Haque, I.; Mobley, D. L.; Lambrecht, D. S.; DiStasio, R. A., Jr.; et al. Current Status of the AMOEBA Polarizable Force Field. *The Journal of Physical Chemistry B* **2010**, *114* (8), 2549-2564. DOI: 10.1021/jp910674d.
(110) Raiteri, P.; Schuitemaker, A.; Gale, J. D. Ion Pairing and Multiple Ion Binding in Calcium Carbonate Solutions Based on a Polarizable AMOEBA Force Field and Ab Initio Molecular Dynamics. *J. Phys. Chem. B* **2020**, *124* (17), 3568-3582. DOI: 10.1021/acs.jpcb.0c01582.
(111) Unke, O. T.; Chmiela, S.; Sauceda, H. E.; Gastegger, M.; Poltavsky, I.; Schütt, K. T.; Tkatchenko, A.; Müller, K.-R. Machine Learning Force Fields. *Chem. Rev.* **2021**, *121* (16), 10142-10186. DOI: 10.1021/acs.chemrev.0c01111.

Supporting Information

Elucidating and contrasting the mechanisms for Mg and Ca sulfate ion-pair formation with multi-level embedded quantum mechanics/molecular dynamics simulations

Jan-Niklas Boyn[1] and Emily A. Carter[1,2,3*]

[1]Department of Mechanical and Aerospace Engineering, Princeton University, Princeton, New Jersey 08544-5263, United States

[2]Princeton Plasma Physics Laboratory, Princeton, New Jersey, 08540-6655, United States

[3]Andlinger Center for Energy and the Environment, Princeton University, Princeton, New Jersey 08544-5263, United States

Figure S1. Comparison of continuous and interval integration of the blue-moon ensemble free-energy gradient to produce free-energy curves (FECs) for Ca-SO_4.

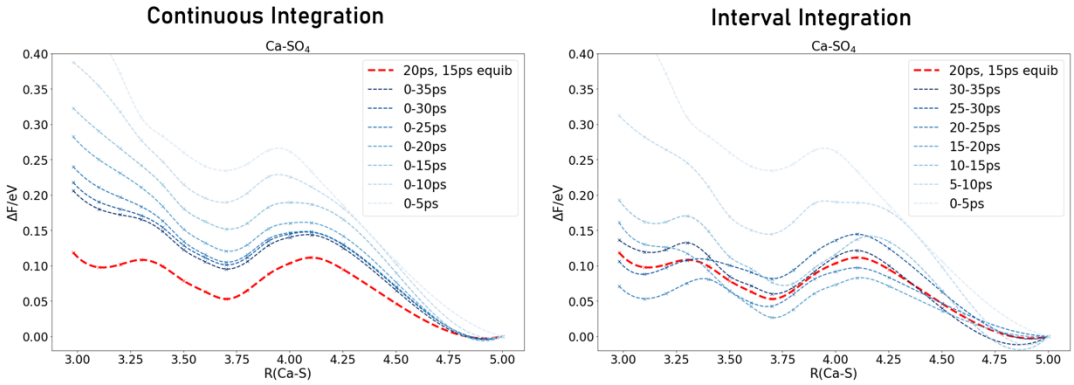

Figure S1. Comparison of Ca-SO_4 ion-pairing FECs obtained from continuous integration (left panel) and interval integration (right panel) of successive 5-ps BME DFT-revPBE-D3BJ-MD trajectories of $Ca(SO_4)(H_2O)_{67}$. Utilization of successive intervals allows for easier identification of required pre-equilibration periods, which should be discarded from the final trajectory in order to avoid a FEC skewed by inclusion of early non-equilibrium, high-energy configurations in the average.

Figure S2. Convergence of blue-moon ensemble gradient for Mg-SO_4 ion pairing and the CN(Mg-O) at TS1.

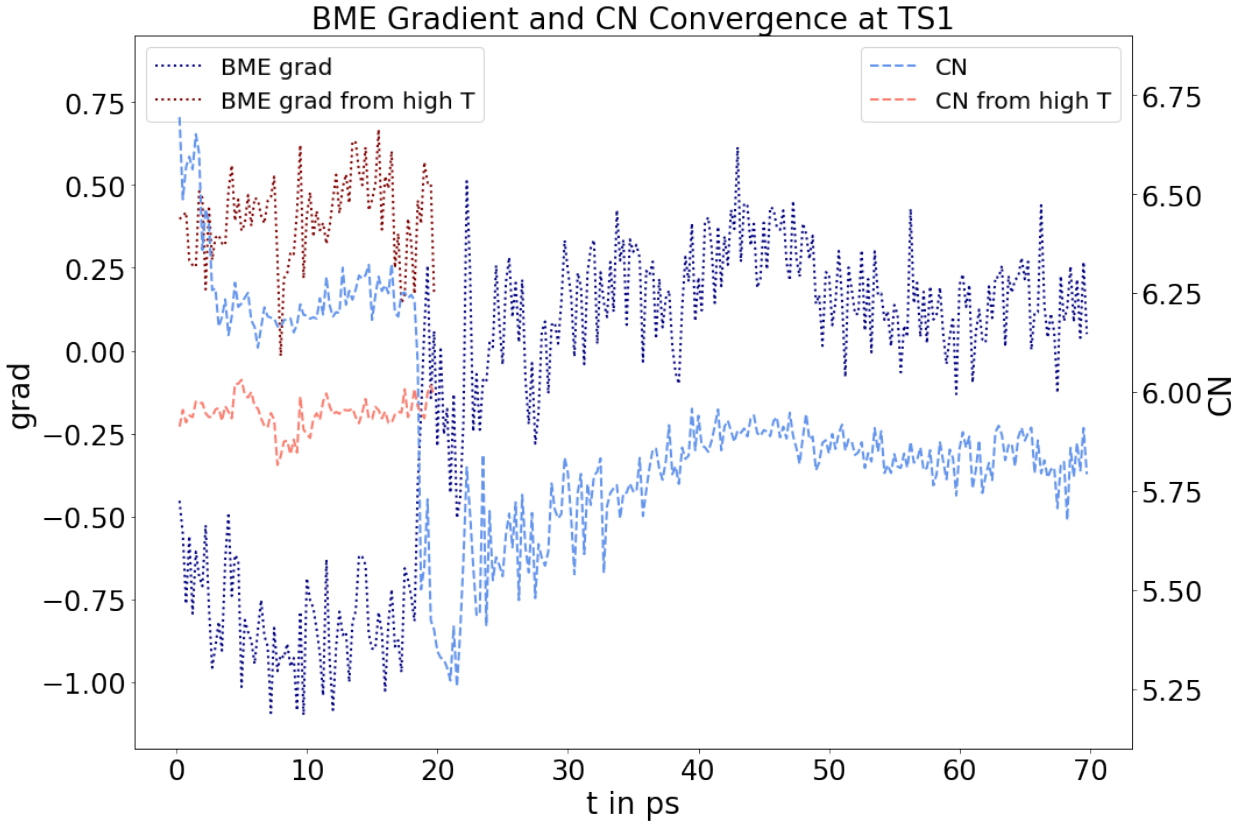

Figure S2. Comparison of the blue-moon ensemble gradient (left axis) along the TS1 (R(Mg-S) = 3.87 Å) trajectory obtained from a 70-ps trajectory (dark blue) without pre-equilibration at 300 K and a 20-ps trajectory at 300 K following 1.25 ps pre-equilibration at 370 K (dark red, denoted "from high T" in legend). Displayed are the averages of consecutive 250-fs intervals (dotted lines). Additionally, CNs averaged over successive 250-fs intervals (right axis), for the non-pre-equilibrated trajectory (dashed line, light blue) and the high-temperature pre-equilibrated trajectory (dashed line, light red) are shown. All data were obtained from simulations DFT-revPBE-D3BJ simulations at 300 K with 0.25-fs timesteps with $Mg(SO_4)(H_2O)_{67}$ supercells. The shorter 20-ps trajectory is able to reach roughly the same values of gradients and CNs as the longer 70-ps trajectory does at longer times simply by virtue of the short high-temperature pre-equilibration.

Figure S3. Convergence of blue-moon ensemble gradient for Mg-SO_4 ion pairing and the CN(Mg-O) at TS2.

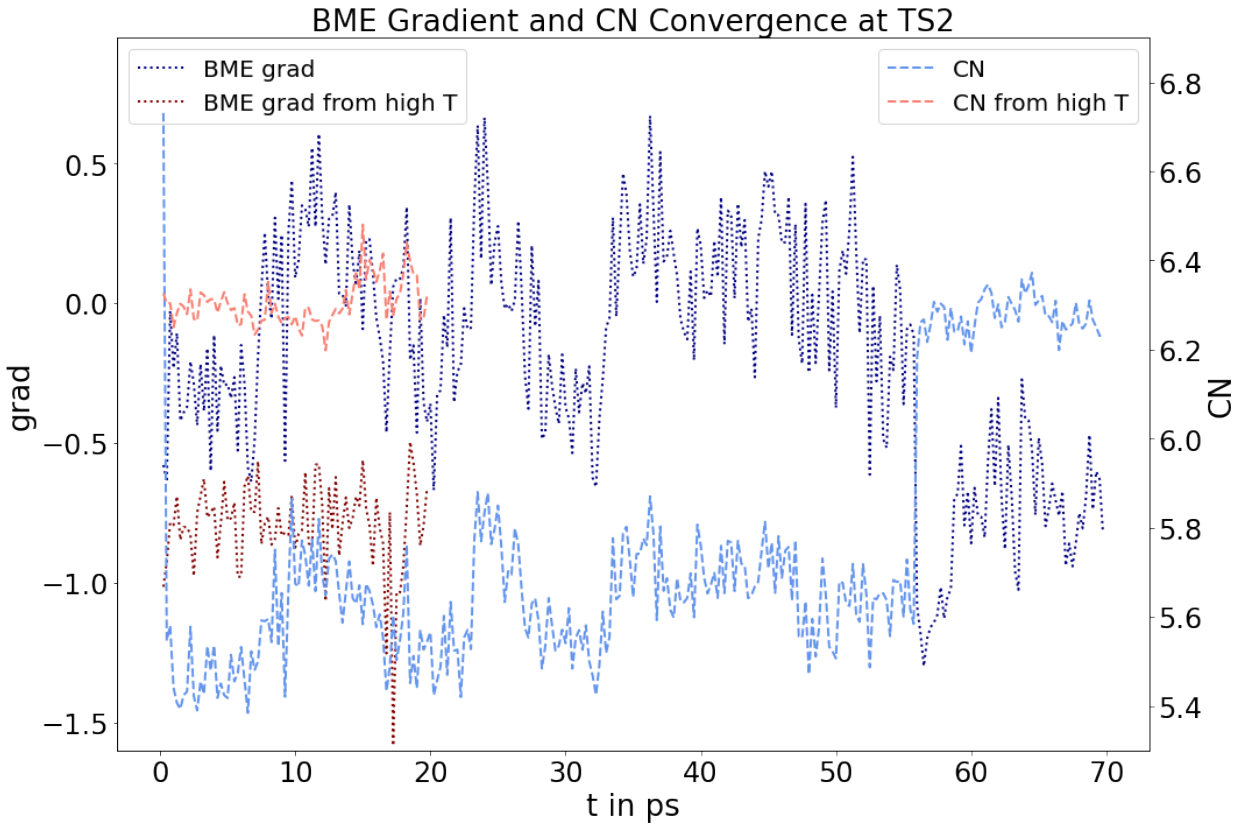

Figure 3. Comparison of the blue-moon ensemble gradient (left axis) along the TS2 (R(Mg-S) = 3.10 Å) trajectory obtained from a 70-ps trajectory (dark blue) at 300 K without pre-equilibration and a 20-ps trajectory at 300 K following 1.25 ps pre-equilibration at 370 K (dark red, denoted "from high T" in legend). Displayed are averages of consecutive 250-fs intervals (dotted lines). Additionally, CNs averaged over successive 250-fs intervals (right axis), for the non-pre-equilibrated trajectory (dashed line, light blue) and the high-temperature pre-equilibrated trajectory (dashed line, light red) are shown. All data were obtained from simulations DFT-revPBE-D3BJ simulations at 300 K with 0.25-fs timesteps with $Mg(SO_4)(H_2O)_{67}$ supercells. The shorter 20-ps trajectory is able to reach roughly the same values of gradients and CNs as the longer 70-ps trajectory does at longer times simply by virtue of the short high-temperature pre-equilibration.